Mixing intensification using sound-driven micromixer with sharp edges

Chuanyu Zhang, Philippe Brunet, Laurent Royon, Xiaofeng Guo

Version of Record: https://www.sciencedirect.com/science/article/pii/S1385894720343631
Manuscript_55895af2ea6faf7bd9fc93a8b8bf78f8

Mixing intensification using sound-driven micromixer with sharp edges

Chuanyu ZHANG[1], Philippe BRUNET[2], Laurent ROYON[1], and Xiaofeng GUO[1,3]

[1]Université de Paris, CNRS, LIED, UMR 8236, F-75006, Paris, France

[2]Université de Paris, CNRS, MSC, UMR 7057, F-75006, Paris, France

[3]Université Gustave Eiffel, ESIEE Paris, F-93162, Noisy le Grand, France

ABSTRACT

Strong acoustic streaming can be generated inside a microchannel near sharp-edge structures. In this study, three Sharp-Edge Acoustic Streaming (SEAS) micromixers with multiple sharp edge patterns actuated by piezoelectric transducers are investigated. Direct Numerical Simulation (DNS) is used to numerically solve the multi-physics phenomenon involving acoustics, fluid dynamics and mass transfer. Experiments are carried out to validate the numerical results by visualization, as well as to evaluate micromixing performance with Iodide-Iodate Reactions. Influence of the sharp edge pattern (i.e. the spacing between individual structures, the number of sharp edges), channel throughput as well as acoustic intensity are studied. The shape of flow streamlines first unveils the interaction between acoustic streaming and main flow, which is shown to be a key for mixing enhancement. Following this, an optimal structure is found among the three mixers which allows achieving a decrease of micromixing time from 0.28 s to 0.03 s. Finally, a comparison with literature on passive mixers confirms the micromixing performance of SEAS mixer in terms of micromixing time at low Reynolds flow.

KEYWORDS

Acoustic Streaming, Sharp-edge, Micromixing, Process intensification, Active enhancement

INTRODUCTION

Mixing is a vital process for operations in microchannels such as chemical reactions, biological syntheses as well as food processing. From the point of view of chemical reactions, homogeneous

and rapid contact between reactants must be realized at the molecular level. As a result, the ability to rapidly create a homogeneous reactant mixture is crucial for the design of microreactors. However, as typical microchannel operations usually involve low-Reynolds number flows, mixing is mainly achieved through molecular diffusion across the interface, especially without external disturbances. Mixing at micro- or millimetric microfluidics is thus very slow for most liquid reagents (DeMello 2006). In such a situation, the mixing efficiency directly affects the quality of a reaction.

Both *passive* and *active* techniques have been used to intensify mixing in microfluidics. Passive techniques optimise the channel geometry, and in turn the flow streamlines, in order to maximize the interface between two fluids. Examples for high and intermediate Reynolds numbers include zigzag-shaped mixing channel (Stroock et al. 2002), tree-like multichannel T-mixer (Guo et al. 2013; Guo et al. 2014), chaotic mixer with 3D L-shape channel or with z-connections (DeMello 2006; Qin et al. 2017). For very low Reynolds numbers, structures like staggered-herringbone grooves have been shown to be effective in mixing (Hossain et al. 2010). While passive mixers only relies on hydrodynamic energy dissipation to improve mixing, extra pumping power is required due to the high pressure drop. The strategy of active mixing, on the other hand, introduces external perturbations (mechanical, ultrasonic, among others) within the fluid. For example, (Li and Kim 2017) designed a water-head-driven microfluidic oscillator to generate periodic fluids bands and achieve rapid mixing. Their experimental study showed that at Re= 0.3∼1 with an external activation of 14∼20 Hz oscillation, complete (macro)mixing can be achieved within mixing distances as short as 1.1 cm ∼ 4 cm. Acoustic vibrations as an active enhancement technique are frequently used to enhance heat and mass transfer (Vainshtein 1995; Setareh et al. 2020; Luo et al. 2018; Shilton et al. 2011; Sritharan et al. 2006; Nam et al. 2018; Rezk et al. 2012). For instance, (Rezk et al. 2012; Shilton et al. 2011; Sritharan et al. 2006; Nam et al. 2018) accelerated the mixing process thanks to chaotic flows induced by Surface Acoustic Wave (SAW). (Orbay et al. 2017; Dong et al. 2015; Zhao et al. 2018; Yang et al. 2020) utilized the effect of the bubble streaming, bubble cavitation under ultrasonic wave to achieve rapid mass transfer process. (Luo et al. 2018) improved micromixing and mass transfer by prescribing ultrasonic wave (20 kHz) in a rotating packed bed reactor. The

collapse of micro bubbles created by ultrasound waves produces microjets and microstreams that enhance micromixing.

Acoustic streaming (AS), a steady flow generated by an acoustic field in a fluid, can potentially be an effective tool to actively enhance mixing. The AS phenomenon is due to second-order nonlinear effects in the coupling between acoustics and hydrodynamics. Historically, acoustic streaming was extensively studied in relatively large fluid volumes like in Kundt's tubes excited by kHz-range acoustic forcing (Hutchisson and Morgan 1931). More recently, AS was investigated in microfluidic channels using transducers in pairs or with reflectors in order to realize a condition of resonance (Lei et al. 2013; Bruus 2012). In the latter situation, the acoustic wavelength has to be of the same order of magnitude as the channel width, which imposes a frequency as high as several MHz. However, recently strong streaming flow around sharp structures has been evidenced (Ovchinnikov et al. 2014; Huang et al. 2013a; Zhang et al. 2019; Zhang et al. 2020b; Doinikov et al. 2020b; Doinikov et al. 2020a) even in the kHz range or lower, attainable even with low-cost piezo-transducers. Contrary to MHz-range AS, the wavelength of audible acoustic wave at several kHz ($\lambda \approx 0.5$ m) is much larger than the typical dimensions of microfluidic devices (smaller than 1 mm). This means the acoustic amplitude within the fluid is homogeneous and the wave has the same phase everywhere. The presence of sharp edges enables the generation of strong acoustic streaming, which would be null in a smooth channel according to the classical Rayleigh theory (Rayleigh 2013). Thanks to its strong transverse (i.e. perpendicular to the main flow) disturbances within a laminar flow, such sound-driven steady flows have promising potential applications in Process Intensification (PI), in particular the micromixing enhancement in continuous microfluidics. For example, (Huang et al. 2013b; Nama et al. 2016) introduced a new type of acoustic streaming near sharp structures into the mixing area, which shows a promising alternative to enhance mixing by low-frequency vibration. Further, the low-frequency sharp-edge AS can be operated under relatively low power input, avoiding local heating from piezoelectric actuators. This makes it particularly adapted to be used in microfluidic devices with low Reynolds number laminar flows, like in a microbiorector, where high-efficient mixing is required while any temperature variation is undesirable (Shanko et al.

2019). Finally, another notable advantage of Sharp Edge Acoustic Streaming mixer is its low-cost system requirement. The most common commercial piezotransdusers (Model ABT-455-RC in our case) can be used and the fabrication of the micro-scale flow chip is relatively easy. Compared with other types of mixers based on magnetic or electric enhancement, the Sharp Edge Acoustic Streaming mixer can be a competitive alternative for industrial applications. This study deals with Sharp Edge Acoustic Streaming applied to mixing, which will be abbreviated as SEAS mixers hereafter.

Acoustic streaming around sharp edges was only recently reported by acoustic or basic fluid mechanics research. Quantitative evaluation of SEAS mixing has not been studied so far. In our earlier experimental (Zhang et al. 2019; Zhang et al. 2020a) and numerical works (Zhang et al. 2020b), the physical mechanisms of streaming flow around a single edge have been thoroughly investigated. Features of SEAS were explored under different conditions, including geometrical (curvature diameters, angles of edge), acoustical (intensity, frequency) and operating ones (flow rate). In (Zhang et al. 2019), we used direct visualisation using fluorescent particles to unveil the streaming generation mechanisms, tracking both the acoustic oscillations and steady acoustic streaming. The mixing process around one single sharp edge is characterized by dye visualisation, confirming the enhancement of macromixing thanks to streaming flow transverse to the main flow. Disturbance distance, vortex size as well as streaming velocity are retained to quantify the streaming intensity. In a more recent study (Zhang et al. 2020b), we gave guidelines on how to obtain strong acoustic streaming with the combination of acoustic and geometrical configurations. We developed DNS (Direct Numerical Simulation) in the finite-element software COMSOL, which proved to provide better predictions than the classical PT (Perturbation Theory) modelling, especially at relatively large forcing. Finally, the dependency of SEAS on fluid viscosity and acoustic frequency was also experimentally studied in (Zhang et al. 2020a). Following our earlier work, to fabricate a channel with an array of sharp edge structures should be effective to considerably enhance mixing. Although several experimental and PT-based simulation studies focusing on chip-scale SEAS mixing have been reported by (Nama et al. 2016; Ozcelik et al. 2014) and, more recently in (Bach-

man et al. 2020), the hydrodynamic streaming mixing enhancement mechanism remains unclear. Namely, several critical questions remain unanswered: i) What is the best geometrical sharp-edge configuration that enables the best mixing performance? ii) From a micromixer application perspective, evaluation of micromixing performance of SEAS through parallel chemical reactions (mainly based on micromixing time), to the best of our knowledge, is still absent in the literature. In particular, micromixing time allows a direct comparison with other type of micromixers (both passive and active), in terms of mixing performance and energy cost. iii) Finally, from a methodology point of view, as we have discussed in our previous study (Zhang et al. 2020b), simulation of SEAS with perturbation method can bring in a considerable error, especially under large acoustic intensity. Developing appropriate numerical scheme to resolve the acoustic-hydrodynamic-mass transfer coupling phenomenon is of high reference value for other acoustofluidics researches.

In summary, the current study intends to go further on the use of SEAS on mixing in microchannel. First, we designed three different SEAS mixers with multiple sharp edges in the aim of unveiling the streaming-mixing interaction and finding the best configuration on mixing performance. Following this design, fluorescence particle visualisation validates the simulation protocol. Then, the effect of streaming on mixing with the three SEAS mixers under specific acoustic conditions are compared. Streamlines of acoustic streaming combined with the main flow, provide valuable clues to design an optimal SEAS mixer. Last, micromixing performance evaluation follows a widely accepted methodology, i.e., Iodide-Iodate reactions. Thanks to performance indicators such as micromixing time and energy dissipation, comparison of SEAS mixer with other previously-reported micromixers illustrates the relative performance of SEAS devices.

MICROMIXER DESIGN AND EXPERIMENTAL PROCEDURE

Y-type SEAS micromixer

A SEAS mixer is made of Polydimethylsiloxane (PDMS) and contains a Y-mixer and a channel with successive sharp-edges put as a network, with a specific distance between each other. The PDMS channel is pre-fabricated using 2D photo-lithography on a wafer (details have been documented in our previous study (Zhang et al. 2019)) and bonded onto a glass slide by oxygen plasma

treatment. Three models (S1, S2, S3) are fabricated and their main geometrical dimensions are detailed in Fig. 1 (b-c). Only the channel section with sharp edge patterns is shown, the Y-mixer being identical for all three models.

Based on our previous study, in which we confirmed that smaller tip angle and smaller curvature diameter of the tip part correspond to stronger streaming flow at same acoustic conditions, the relatively small tip angle $\alpha = 30^{\circ}$ is adopted (the curvature diameter $\delta = 3.1 \pm 1\mu m$). The reason why smaller tip angle is not used here is that, during the process of fabrication, the tip part of the sharp edge might split. This leads to the inhomogeneous curvature diameters and various magnitudes of the streaming flow within one channel. If the stability of the geometrical parameter for single sharp edge can not be guaranteed, it is not possible to further investigate which parameters can affect the mixing performance for multiple sharp edges channel. After determining the structure of single sharp edge, we focus on the density of the sharp edges within a constant length of mixing area. Three different types of channel: i) no space between two consecutive sharp edges on one side $d = 100\mu m$ (S1); ii) interval equal to width of one single sharp edge: $d = 200\mu m$ (S2); iii) much larger space interval: $d = 300\mu m$ (S3).

To provide an acoustic field in a frequency range between 2 and 3 kHz, a piezoelectric transducer is glued with epoxy resist on the glass coverslip slide, next to the channel (Fig. 1-b). After a careful tuning of f corresponding to one of the resonances of the transducer, streaming clearly appears near each and every tip. The two main control parameters are then the acoustic amplitude (or velocity) and the flow-rate.

Specifically, the experimental setup shown in Fig.1 (a) is composed of two syringe pumps (Newtown Company & Co) that enable the continuous injection of fluid from two syringes, under well-controlled flow-rate via the two inlets through the channel. A function generator (Model 33220A Arbitrary waveform generator, Agilent) with a home-made adjustable power amplifier provides the signal supplied to the piezoelectric transducer (Model ABT-455-RC, RS Components). The flow visualization is achieved by a binocular microscope together with a fast camera (Motion-BLITZ Cube4, Mikrotron). The piezoelectric transducer (diameter 35 mm and height 0.51 mm)

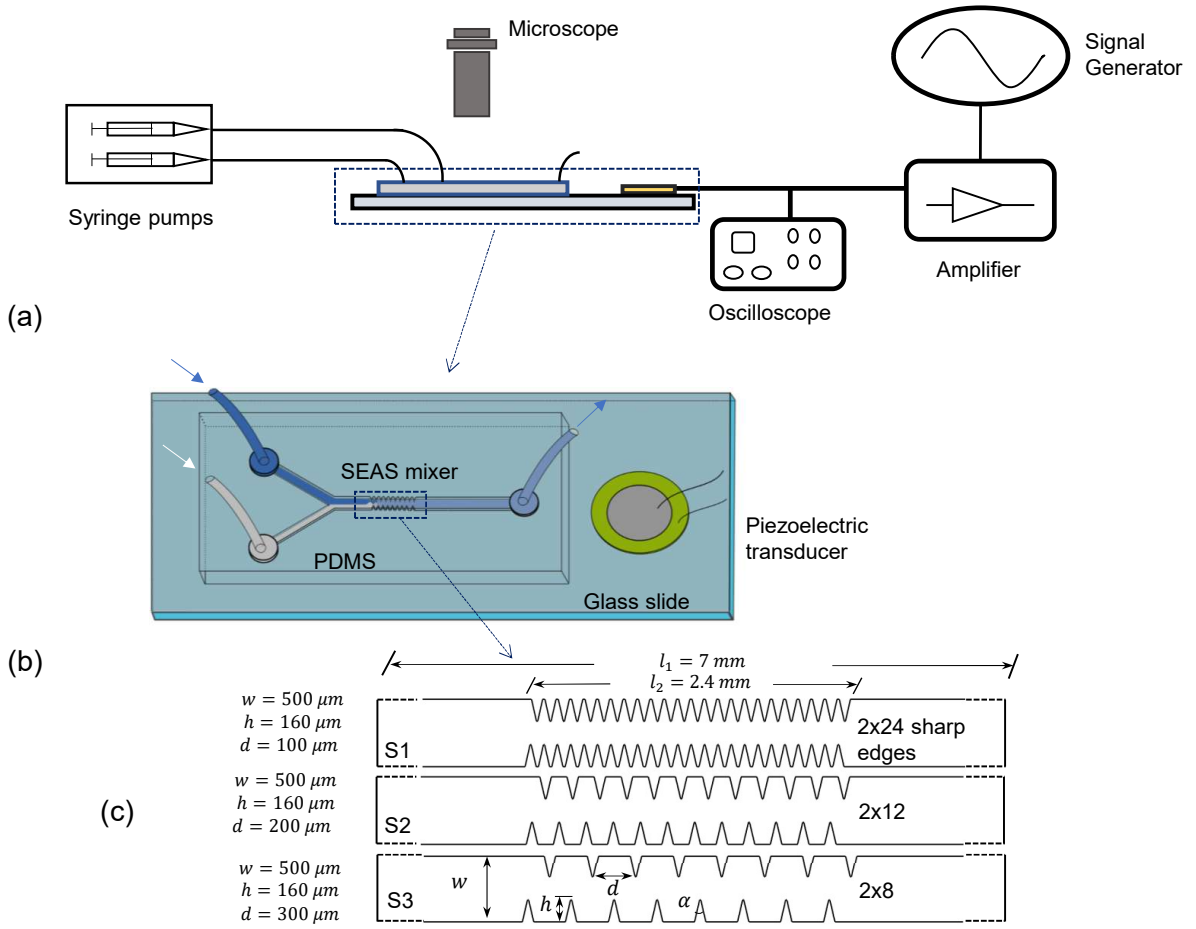

Fig. 1. Schematic of the experiment in this study: (a) Experimental setup with (b) the micro-channel and the transducer glued on the upper coverslip. (c) Three different geometry structures tested, with n_s = 24, 12 or 8, being the number of sharp edges on each side, varying with the distance d between the tip of two consecutive edges.

delivers acoustic vibrations to the glass slide and to the whole channel stuck onto it, at various resonance frequencies from 0.1 kHz up to 5 kHz. We chose to operate at a frequency f = 2.5 kHz corresponding to one of these resonance peaks. It turns out that the best operating conditions in terms of streaming flow were obtained at this frequency.

The relation between the acoustic vibration amplitude v_a (v_a refer to the norm of $\mathbf{v}_a$) in terms of velocity and input voltage V_{pp} is shown in Fig.2. It turns out that v_a shows a rather linear

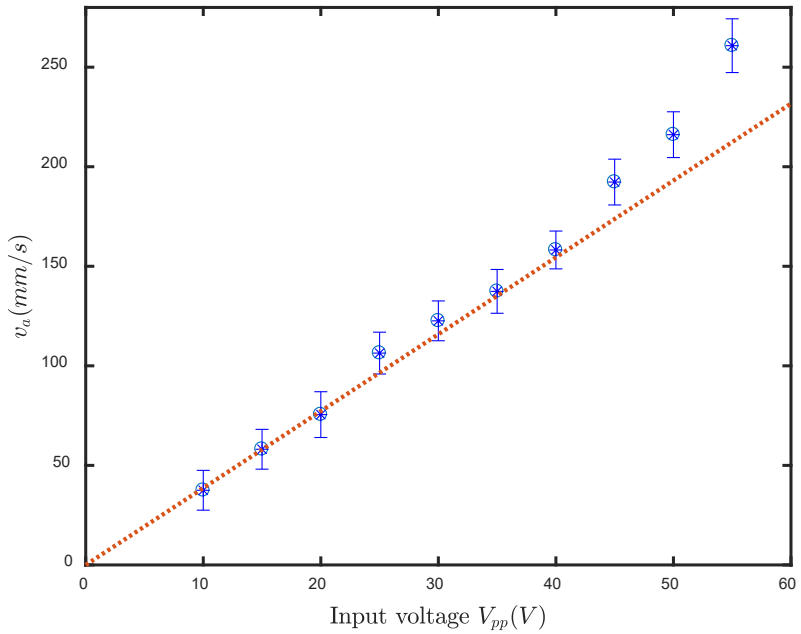

Fig. 2. Acoustic vibration amplitude varies with input voltage

variation with V_{pp}, except in the upper range of values, typically below 45 Volts. In practice, most of the results shown in this study was obtained in the range $V_{pp} < 45V$. We opted to choose v_a as the control parameter that quantifies the amplitude of the applied acoustic field. Complementary measurements showed a rather complex field of vibrations on the glass slide (Zhang et al. 2019). Here v_a directly quantifies the real acoustic excitation, which is effective inside the channel and enables comparisons between different experimental studies. Here, it should be noted that v_a is measured far away enough from the sharp edge, and is adopted as the value of v_{ab} in the simulation part. The details of the measurement of v_a are given in a previous study (Zhang et al. 2019).

Macromixing measurement

The visualisation of the macromixing between two fluids of different colors helps to track the mixing process. One fluid is a mixture of Methylene blue dye (Fisher BioReagents) into deionized water, while the other one is pure deionized water. Captured image sequences are then used to validate the numerical protocol (This will be presented later). To qualify the macromixing

performance, the normalized concentration is introduced in this study to describe the concentration profile along the width of the channel at a specific position. The normalized concentration is obtained based on the Beer-Lambert Law:

$$C_n = ln\frac{I_0}{I}/ln\frac{I_0}{I_b} \tag{1}$$

where C_n stands for the normalized concentration; I_0 is the grey value of pure water; I_b is the grey value of the unmixed blue dye liquid; I is the grey value of pixels.

Micromixing measurement procedure

General visualization techniques only show the mixing layers between fluids above the micron scale, which is the typical scale of *macromixing*. However, at a molecular scale, especially when mixing is associated with chemical reactions, quantitative characterization to evaluate the *micromixing* becomes necessary. Iodide-Iodate reactions is a commonly accepted protocol to this aim. Also named Villermaux-Dushman method, the protocol involves two competing parallel reactions at two distinct reaction rates : a quasi-instantaneous neutralization reaction and a redox reaction of several order of magnitude slower in terms of reaction rate than the former. This allows to characterize mixing at the molecular scale through the yield of Iodine (I_2) molecules in the final effluent. It is thus particularly useful to interpret the mixing process as a chemical probe. Details of the method are given in the Appendix I.

Additionally, combined with a tubular reactor model IEM (Interaction by Exchange with the Mean), the Iodide-Iodate protocol allows to access micromixing time (t_m). This enables to conduct a direct and quantitative comparison of performance between different micromixers (Falk and Commenge 2010).

Chemicals and test procedure

Precautions are necessary in the choice of reactant concentrations with which the Absorbance Unit (A) given by the spectrophotometry under all operation conditions should fall in the range $0.1 < A < 3$. This guarantees to remain in the linear range, that enables the use of the Beer-Lambert

law to determine the molar concentration of tri-iodide. To this end, we adopt a trial-and-error approach to find the best choice for concentration, as shown in Tab.1. To cope with the small throughput (Q_c ≤12 µL/min) issue, we use a high-precision micro-cuvette (Hellma, QS105 model, 50 µL, light path 10 mm) to collect the solution as close as possible from the outlet. Each test is conducted under stationary conditions, which is appreciated from direct visualisations. The sample is then put in spectrometer (Jenway 7310) once the cuvette is sufficiently filled.

	$[H^+]$	[KI]	$[KIO_3]$	[NaOH]	$[H_3BO_3]$
C [mol/L]	0.03	0.016	0.003	0.045	0.045

TABLE 1. Concentration set used to characterize micromixing

Once the spectrometer results are obtained, we use Beer-Lambert law to determine the I_3^- yield (concentration $C_{I_3^-}$). To quantitatively analyze the micromixing process, the Segregation Index (X_s) and Micromixing time (t_m) are determined through the IEM model (Details of this model are put in Appendix II). For each test, values of t_m and X_s are obtained through the measured concentration I_3^- collected at the outlet. The relation between X_S and t_m at given reactant concentrations is shown in the Appendix II

Segregation Index

As a quantitative indicator in the Iodide-Iodate reactions scheme, Segregation Index X_S can characterize the mixing efficiency through a given micromixer under a fixed reactant concentration. It is defined by the ratio of the iodine yield (Y) in a test (real case) to the maximum yield of iodine (Y_{ST}) in the case of most inefficient mixing (total segregation case), as in Eq.2.

$$X_S = \frac{Y}{Y_{ST}} \tag{2}$$

In the case of total segregation, the two competitive reactions R1 and R2 (shown in Appendix I) are quasi-instantaneous with respect to the micromixing time, supposed to be infinitely long. Conversely, ideal micromixing implies arbitrarily short micromixing time. Thus, with ideal mi-

cromixing $X_S = 0$, and with total segregation $X_S = 1$. Partial segregation follows the definition $X_S = Y/Y_{ST}$ and it results in a value between 0 and 1. The calculation of Y and Y_{ST} involves all reactant concentrations and it follows the procedure described in the Appendix I.

Micromixing time

Different Segregation Indices X_S can be achieved with different presumed t_m following the procedure in Appendix II. Then the relation between the X_S and t_m can be built up, as shown in Fig.14 (Appendix II), through which, t_m under different conditions can be determined with the segregation index X_S measured by experiment. For t_m, its value can be compared with those under various experimental conditions, like different initial ions' concentrations. However, the value for X_S depends not only on the mixing performance itself but also on the initial ions concentration. Previous investigations opted for concentration values according to the specific mixer design. Hence direct performance comparison between different micromixers by segregation index is not relevant. In such a situation, the only reliable criteria to estimate the mixing performance has to rely on the micromixing time, instead of the segregation index. Therefore several recent comparative micromixing studies have been conducted with the above method (Qin et al. 2017; Li et al. 2019).

THEORETICAL BACKGROUND

Origin of Sharp-Edge Acoustic Streaming (SEAS)

The sharp-edge AS in this study uses acoustic wavelength $\lambda_c = c/f$, of the order of half a meter, hence much larger than the characteristic flow size in microfluidics. There are three velocities involved : acoustic velocity $\mathbf{v}_\omega = Re[\mathbf{v}_a e^{i\omega t}]$ (fluid vibration induced by piezo-transducer, time-dependent part, $\mathbf{v}_a$ is the complex amplitude, $Re[\cdot]$ denotes the real part of a complex term), streaming velocity $\mathbf{v}_s$ (steady-state streaming) and mainstream velocity $\mathbf{v}_0$. All of them being much lower than the sound speed (c=1430 m/s in water), the flow is thus incompressible. According to the classical Perturbation Theory (PT), the steady streaming velocity can be theoretically solved through the time-averaged second-order momentum and continuity equations in Eq.3 and Eq.4 (Ovchinnikov et al. 2014).

$$(\mathbf{v}_s \cdot \nabla)\mathbf{v}_s = -\frac{1}{\rho}\nabla p_s - F_s + \nu\nabla^2\mathbf{v}_s \tag{3}$$

$$\nabla \cdot \mathbf{v}_s = 0 \tag{4}$$

where v_s is the second-order time averaged velocity (streaming flow); $F_s = \frac{1}{2}Re[< (\mathbf{v}_a \cdot \nabla)\mathbf{v}_a^T >]$ is the time averaged inertia term as a result of the first-order oscillatory field. And it's also named averaged *Reynolds Stress Force* (Lighthill 1978), it represents the driving force of the streaming flow in the fluid bulk acting within and beyond the viscous boundary layer.

From the form of F_s, it is clear that a homogeneous acoustic field cannot generate any streaming flow along straight and smooth walls, as the effective force would be null (Ovchinnikov et al. 2014; Zhang et al. 2019; Zhang et al. 2020b). Within the boundary layer, the oscillations are subjected to spatial variations and vanish along the wall due to the no slip boundary condition. Despite the spatial variations of $\mathbf{v}_a$, the direction of oscillations keeps parallel to the straight horizontal wall, so that F_s remains null (Ovchinnikov et al. 2014; Zhang et al. 2020b). However, the presence of sharp edge structures with strong local curvature on the channel walls induces sharp spatial variations in the acoustic fluid oscillation near the tip (Zhang et al. 2019; Zhang et al. 2020b), which makes F_s non-zero locally. As sketched in Fig.3-(a) for a single sharp edge in a channel, the vibration is uniformly distributed in the channel except for the local zone close to the sharp edge. More specifically, close to the tip, both the orientation of the acoustic field and the vibration amplitude provide favorable conditions to induce an intense streaming force F_s. Far enough from the tip, typically at a distance of a few boundary layers, the force becomes null or negligible. Therefore, the sharp edge induced non-uniformity of the acoustic field makes acoustic streaming at relatively low frequency (several kHz) possible.

Since the streaming force F_s generates a jet shooting from the sharp edge in the transverse direction, a pair of counter-rotating vortices is in turn generated as shown in Fig.3(b). These counter-rotating vortices in the fluid bulk can induce significant disturbance to the main flow at a distance much larger than the boundary layer thickness. Outside the boundary layer, the streaming

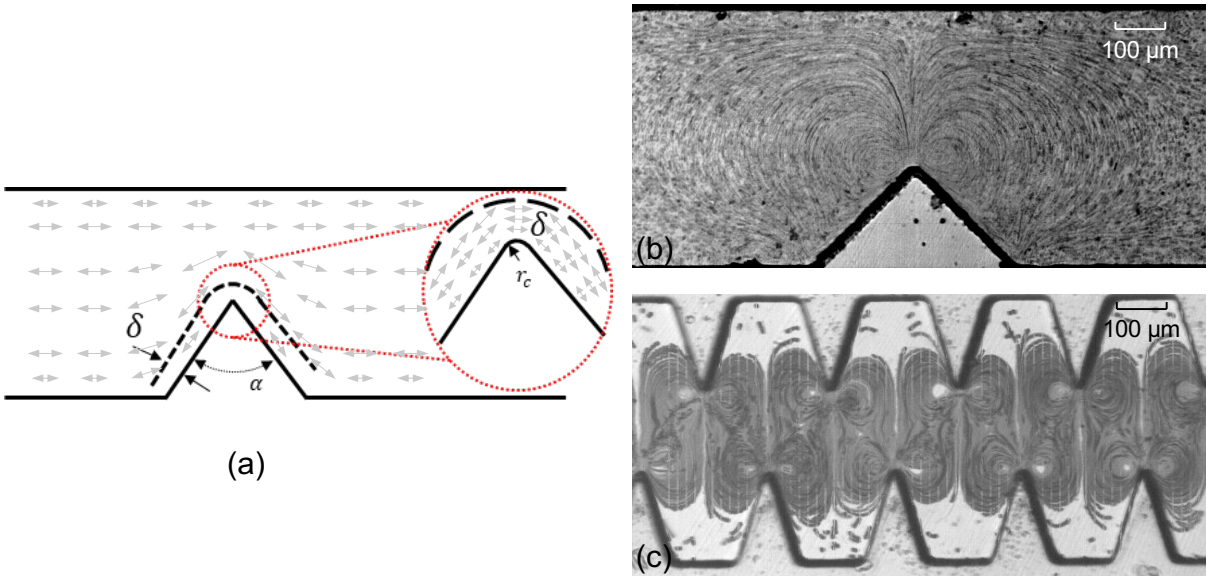

Fig. 3. Origin of the acoustic streaming around the sharp edge. (a) Sharp edge of angle α and curvature diameter $2r_c$ inside a channel, δ shows the boundary layer thickness; Grey arrows represent acoustic oscillations driven by piezoelectric transducer. Particle visualisation of (b) single sharp-edge and (c) multiple sharp-edge acoustic streaming.

flow interacts with the main flow, and is susceptible to enhance the advection and mixing of species along the channel. Enhancement of mass transfer of two parallel fluids is thus possible. From the basic flow visualisations for a single sharp edge, our study extends to the case of multiple sharp edges (as shown in Fig.3-(c)). Our expectations are that the interaction and cooperative effects of these several transverse flows and vortices should be suitable for mixing enhancement.

Numerical modelling of acoustic streaming

Although being particularly adapted in qualitative interpretation of the origin of acoustic streaming near sharp edges, the classical Perturbation Theory (PT) fails to accurately predict the magnitude of the streaming velocity. The main reason lies in the particularity of sharp edge streaming for which the streaming velocity $\mathbf{v}_s$ can be of the same order of magnitude as the vibration velocity $\mathbf{v}_a$ (Zhang et al. 2019), which is not the case for classical Rayleigh streaming. As discussed above, the velocity field $\mathbf{v}$ and pressure field p can be separated to three parts, shown in Eq.5 and 6. Then the momentum equation Eq.7 can be separated into two parts : the oscillatory terms (Eq.8) and the

steady terms (Eq.9). The PT method simplifies the coupling between $\mathbf{v}_a$ and $\mathbf{v}_s + \mathbf{v}_0$ by neglecting the following terms in Eq.8 : $((\mathbf{v}_s + \mathbf{v}_0) \cdot \nabla)\mathbf{v}_a + (\mathbf{v}_a \cdot \nabla)(\mathbf{v}_s + \mathbf{v}_0)$. As a consequence, our earlier work (Zhang et al. 2020b) showed inaccurate resolution of the streaming velocity from PT and the coupling terms in the context of sharp edge streaming are to be considered.

$$\mathbf{v} = \mathbf{v}_0 + \mathbf{v}_\omega + \mathbf{v}_s,\ \mathbf{v}_\omega = Re(\mathbf{v}_a e^{i\omega t}) \tag{5}$$

$$p = p_0 + p_\omega + p_s,\ p_\omega = Re(p_a e^{i\omega t}) \tag{6}$$

$$\begin{aligned} &\frac{\partial \mathbf{v}_\omega}{\partial t} + \left\{[\mathbf{v}_s + \mathbf{v}_0 + Re(\mathbf{v}_a e^{i\omega t})] \cdot \nabla\right\}[\mathbf{v}_s + \mathbf{v}_0 + Re(\mathbf{v}_a e^{i\omega t})] \\ &= -\frac{1}{\rho}\nabla[p_s + Re(p_a e^{i\omega t})] + \nu\nabla^2[\mathbf{v}_s + \mathbf{v}_0 + Re(\mathbf{v}_a e^{i\omega t})] \end{aligned} \tag{7}$$

$$i\omega\mathbf{v}_a + ((\mathbf{v}_s + \mathbf{v}_0) \cdot \nabla)\mathbf{v}_a + (\mathbf{v}_a \cdot \nabla)(\mathbf{v}_s + \mathbf{v}_0) = -\frac{1}{\rho}\nabla p_a + \nu\nabla^2\mathbf{v}_a \tag{8}$$

$$((\mathbf{v}_s + \mathbf{v}_0) \cdot \nabla)(\mathbf{v}_s + \mathbf{v}_0) + \frac{1}{2}Re[(\mathbf{v}_a \cdot \nabla)\mathbf{v}_a^*] = -\frac{1}{\rho}\nabla p_s + \nu\nabla^2(\mathbf{v}_s + \mathbf{v}_0) \tag{9}$$

Recently, we carried out simulations by directly solving the Navier-Stokes equation with periodic boundary conditions, using DNS (Zhang et al. 2020b). With this technique, the time-dependent variable $\mathbf{v} = Re(\mathbf{v}_a e^{i\omega t}) + \mathbf{v}_s + \mathbf{v}_0$ at a given time-step can be obtained by directly solving Eq.(7) in a two-dimensional domain with periodic boundary conditions : $\mathbf{v}_b = Re(\mathbf{v}_{ab} e^{i\omega t}) + \mathbf{v}_{0b}$. $\mathbf{v}_{ab}$ is the $\mathbf{v}_a$ at boundary, and $\mathbf{v}_{0b}$ is the boundary velocity corresponding to channel throughput (cf Fig. 4 (a)). Then the steady velocity $< \mathbf{v} >$ is available by time averaging $\mathbf{v}$ over several acoustic periods. Details about DNS implementation can be found in (Zhang et al. 2020b).

$$\bar{\mathbf{v}} = \mathbf{v}_s + \mathbf{v}_0 = \frac{\int_0^T \mathbf{v} dt}{T} \tag{10}$$

where $\mathbf{v}_0$ is the steady velocity field corresponding to channel throughput, and $T = \frac{1}{f}$ is the acoustic wave period.

Based on the above methodology, simulations of the velocity field can be proceeded as the first step. Then, species transport (macromixing) can be included by adding the classical mass transport

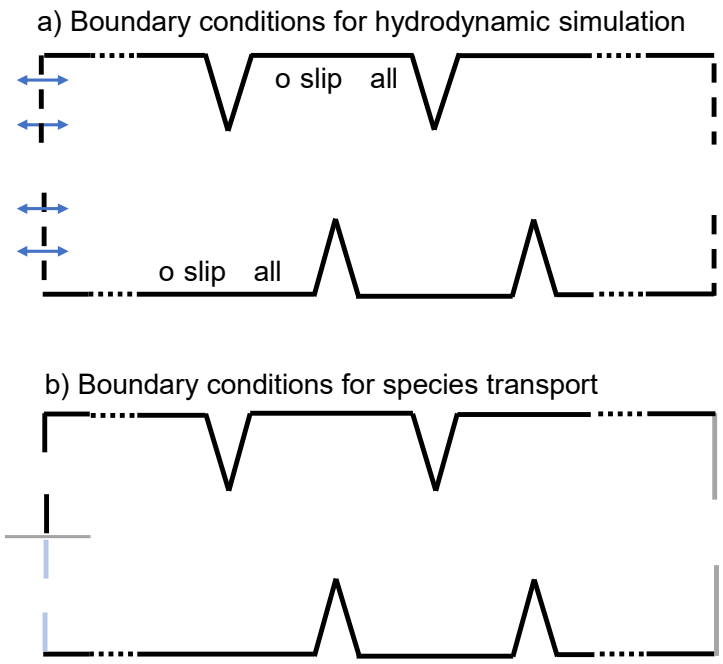

Fig. 4. Boundary conditions used in the DNS modeling

equation Eq.11 in a second step with species concentration boundary conditions as shown in Fig.4 (b).

$$- D_i \Delta C_i + \mathbf{v} \cdot \nabla C_i = 0 \tag{11}$$

where D_i is the diffusion constant of the i_{th} species. C_i refers to the molar concentration of the i_{th} species. Physically, the equation represents equal value of diffusive part $D_i \Delta C_i$ with convective part $\mathbf{v} \cdot \nabla C_i$ in a steady-state source-less diffusion-convection phenomenon.

It is worth noting that in this step, we use the mean steady velocity $\bar{\mathbf{v}}$ from the hydrodynamic solution as $\mathbf{v}$ in the convective term. In other words, the periodic acoustic oscillation velocity is considered to have no influence on mixing. First, this assertion is based on our experimental visualization to a smooth channel, showing no mixing enhancement effect without acoustic streaming even with acoustic ON. Indeed, the first order vibration, as it mainly follows the longitudinal direction of the mixing channel hence in parallel to the main flow, does not increase the transverse advection of the two species.

Specifically, two solutions with $C_1 = 1$ and $C_2 = 0$ allow to directly obtain dimensionless concentration between 1 to 0 (mixing degree). Then macromixing process between two miscible fluids intensified by streaming phenomenon in the micro channel with sharp edges array can be simulated.

Mixing enhancement by streaming

The present study addresses an advection dominant mixing process which, without any acoustic streaming, would be extremely slow. More specifically, the channel flow is characterized by very low Re, ranging from 0.12 to 0.72 for the tested flow rates of 2 μL/min to 12 μL/min, and considering a channel with smooth walls. It is determined by $Re = \frac{\overline{v_0} D_h}{\nu}$, with D_h being the hydraulic diameter given by $4A/p$; $\overline{v_0}$ is the mean velocity corresponding to the channel flow-rate divided by its sectional area. In terms of relative importance between advection and diffusion, the Peclet number $Pe = Re \cdot Sc$ takes values above 1, typically ranging between 61 and 364, with Sc is the Schmidt number equal to 502 for Methylene dye in water. This implies that the convective transport along the flow direction dominates diffusion in the transverse direction. Under these conditions, and with a laminar Hagen-Poiseuille flow with parabolic velocity field along the channel axial direction, the mixing of the two fluids is strongly limited along a distance as short as $L/w = 14$ with L=7 mm and w=0.5 mm. Jets and vortices driven by acoustic streaming are expected to circumvent this limitation.

RESULTS AND DISCUSSIONS

Validation of numerical results

Figure 5 shows the validation of numerical results by experimental visualisation (macromixing) with blue dye. The S1 mixer is used under the following operation conditions: v_a=85 mm/s, Q_c=8 µL/min. For the mass transfer, a mass diffusivity of $D = 2.49 \times 10^{-9} m^2/s$ (Leaist 1988) is used in the simulation.

Concentration evolution contours in Fig.5b) and c) obtained both experimentally and numerically show satisfactory agreement, which is also the case over the whole range of tested values for v_a. Similar grey level distribution - thus tracer concentration, are shown before, through and

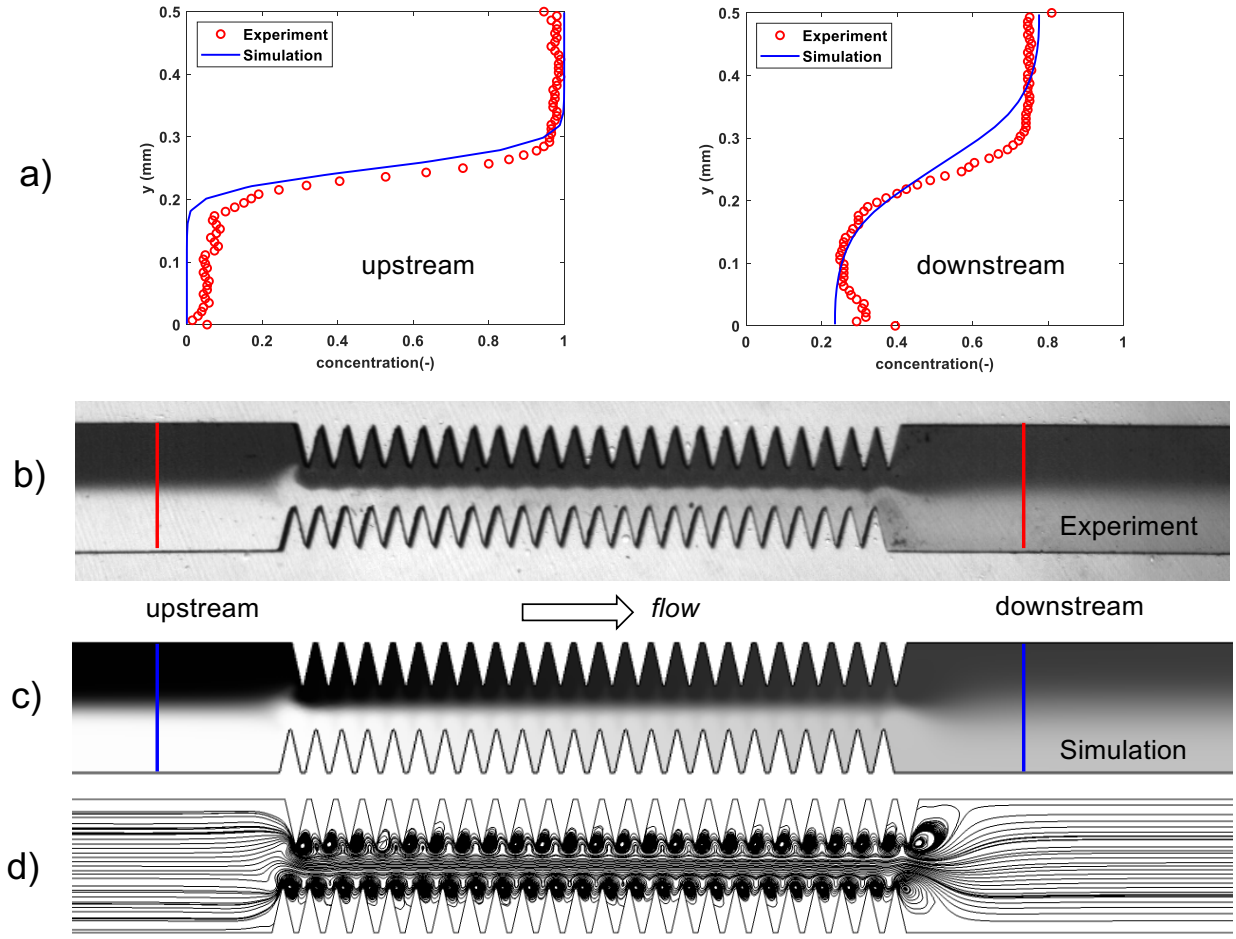

Fig. 5. Experimental validation of numerical results on active acoustic streaming driven mixing of two miscible fluids (water, water with Methylene blue) using micromixer S1. a) Concentration profiles before (upstream, left) and after (downstream, right) the SEAS mixing channel. The concentration profiles are taken at a distance of 0.5 mm before and after the first/last sharp edge, where the profiles are not perturbed by remaining vorticity, b) Experimental concentration evolution in the mixing channel, c) Same concentration field obtained numerically, d) Flow streamlines obtained numerically. The acoustic amplitude is v_a=85 mm/s and the flow rate is Q_c=8 µL/min. Concentration is normalized according to grey-scale contrast between two inlet fluids, i.e., from 0 to 1.

after the sharp-edge network. Upstream, the two fluids are clearly separated at the centerline of the channel. This is consistent with the advection-dominant flow (Pe$\gg$1) under low-Reynolds laminar regime (Re<1).

As a quantitative comparison, Fig.5-a) confirms the accuracy of the numerical simulations by concentration profiles respectively at the *upstream* and *downstream* locations of the mixing zone. Before entering the sharp-edges zone, the fluids are perfectly separated and the dye normalized concentration is either close to 0 or to 1. After crossing the sharp-edges region, the two fluids are brought closer to the 50%-50% line (ideal mixing). However, under a relatively low acoustic intensity (v_a=85 mm/s), perfect mixing is not well achieved downstream. For this S1 mixer at least, the generated AS is too weak. It should be noted that in our experimental visualisation process, surface roughness and noise in the low concentration regime lead to a small error of grey level I_0, which then influences the concentration calibration and accounts for the slight discrepancy between simulations and experiments in Fig.5(a). At higher concentrations, however, we obtain satisfactory validation results..

In addition, the steady-state flow streamlines, resulting from the coupling between the main longitudinal flow and the acoustic streaming (disregarding acoustic velocity here), and under the same flow and vibration conditions, are shown in Fig. 5-d). At the centerline, the velocity remains roughly parallel to the main flow and the interface area between the two fluids is only slightly thickened by the space-periodic bending of the streamlines. Moreover, the triangular areas between two adjacent sharp edges do not look disturbed by acoustic streaming. These *dead zones* show a clear limitation of mixing, and are to be avoided from a mixing enhancement prospective.

Based on the experimental validated numerical scheme, we conducted a series of simulations with the three different mixers shown in Fig.1, in the aim of finding the optimal geometry of sharp-edge mixing channels, under the same acoustic and throughput conditions.

Performance comparison of SEAS mixers

Figure 6 shows concentration maps obtained from numerical simulations with the three SEAS mixers, under the same operating conditions : acoustic amplitude v_a=130 mm/s, channel throughput

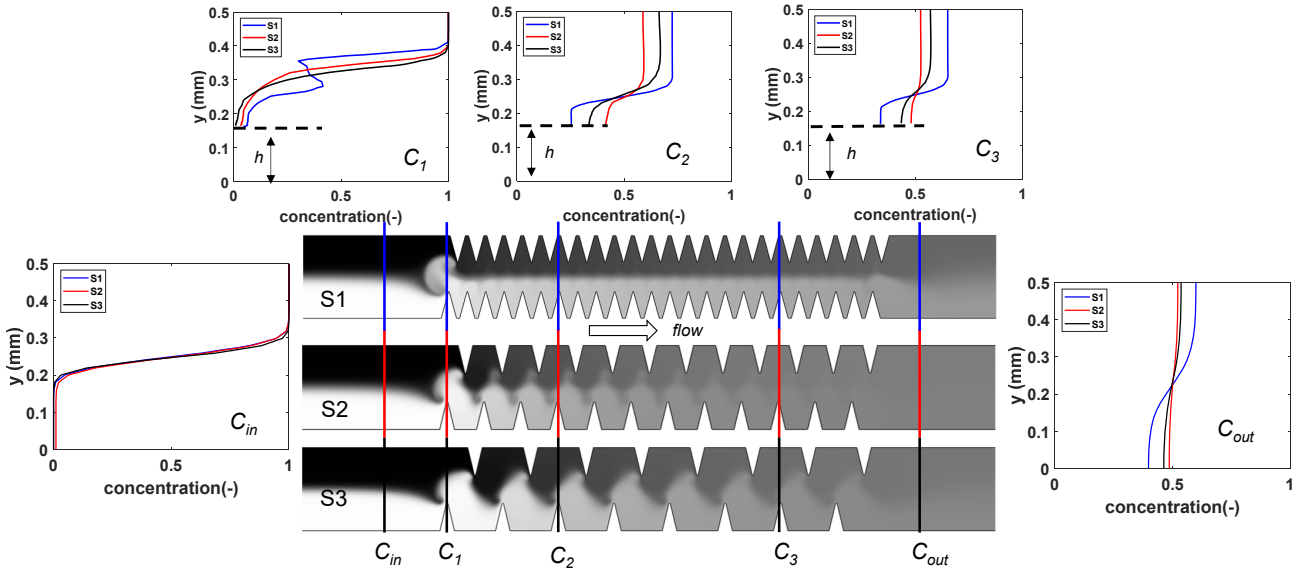

Fig. 6. Comparison of mixing performance of three micromixers S1/S2/S3. Concentration grey level maps from numerical simulation under the same following conditions: v_a=120 mm/s and Q_c= 8 µL/min. Cross-section concentration profiles are shown as inserts, for different longitudinal locations. Concentration curves from C_{in} to C_{out} quantitatively confirms the performance order from S2>S3>S1, with an identical inlet condition C_{in}. Normalized concentration, from 0 to 1, is utilized here.

Q_c=8 µL/min. From these maps, one extracts the concentration profiles along the channel width, at five representative longitudinal positions, shown as inserts in Fig.6, with C_{in} and C_{out} being respectively the profiles at the inlet and outlet.

The cross-section concentration profiles extracted at different longitudinal locations, and especially C_{out}, suggest that S2 should be the optimal sharp-edge network for better mixing performance.

The three grey level maps shown in Fig. 6 comparatively illustrate the performances of the three mixers. Under the same flow conditions and inlet concentration profile C_{in}, the mixer S2 achieves the best mixing efficiency (evaluated at the outlet) while S1 corresponds to the worst one. At the entrance area, just before the first sharp edge, a disturbed concentration distribution C_1 can be shown and S1 seems to provide stronger disturbances than S2 and S3. Further downstream, S2 shows more twisted concentration profiles and better mixing performance in the whole area

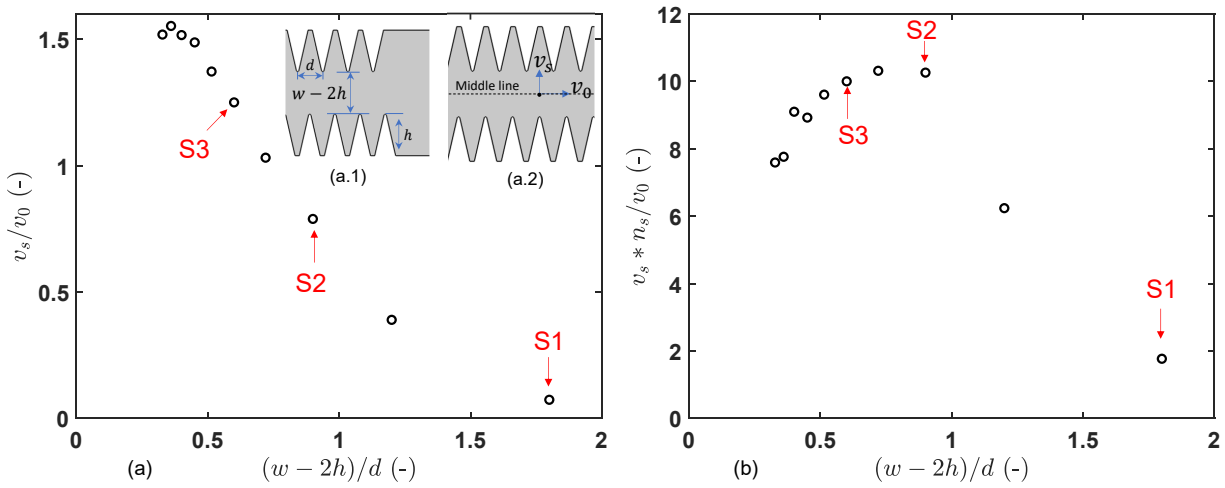

Fig. 7. Parametric simulation of mixing enhancement indicators by adjusting sharp edge patterns. Ratio v_s/v_0 versus $(w-2h)/d$ for different sharp-edge micromixers (left). Quantity $n_s \times v_s/v_0$ versus $(w-2h)/d$, showing S2 as an optimal geometry for mixing (right). The sharp edge section (l_2) is kept the same for the variety of edge densities.

between C_1 and outlet. A closer examination of the cross-section profiles and grey map reveals that S2 and S3 seem to allow larger vortices-induced mixing within the spaces between sharp edges in the middle of the channel. For the case of S1, it seems that the disturbance to the fluids is hindered by the narrow space between two opposite structures. Conversely, S2 and S3 enable fluids to *jump out* from each sharp edge to reach the zones between two consecutive edges at the opposite wall. Therefore, despite S1 corresponds to the densest sharp-edge network, the small space between edges limits the full development of the streaming flow. As a result, the disturbed flow by AS vortices are within each local fluid instead of being useful for the mixing of them. The first sharp edge of S1, though, seems to play a major role in the mixing before the channel. Strong advection can be achieved at this entrance when the mainstream is subjected to a strong transverse streaming, thus mixing can be enhanced. Also, this effect appears with S2 and S3.

Based on the above results and discussions, the space between consecutive edges seems to play a important role in the mixing process. As shown in Fig.7, at this stage though, we can propose a coarse estimation for the optimal performance of the S2 mixer from purely kinetic and geometrical arguments. This optimum results from a compromise between the streaming velocity generated

from a single sharp edge, and the length of the mixing area - or the number of mixing elements. In short, if the pattern is too narrow, each streaming jet shall not have enough space to develop toward the opposite wall, reducing the effective transverse velocity. In contrary, if the pattern is too loose, there will be too few transverse streaming jets and the mixing efficiency shall drop.

The orientation angle of the jet is roughly estimated by $\arctan(\frac{v_s}{v_0})$, and this angle should fit with $\arctan(\frac{w-2h}{d})$, which is roughly the angle of the segment relating two consecutive edges at opposite walls. Let us remark that v_s is here evaluated from numerical simulations for the different values of d, taking a typical averaged value from the jet centerline. Dropping the arctan(), we plot the quantity $\frac{v_s}{v_0}$ versus $\frac{w-2h}{d}$ (see Figure 7), confirming that the transverse disturbances are stronger for S2 and S3 geometries. Remarkably, there is a sharp drop beyond $\frac{w-2h}{d} > 1$, i.e. for denser edge structures like S1. In terms of global mixing efficiency, the number of sharp edges also matters, so that the narrowest pattern on the plateau (S2) represents an optimum of efficiency. This is also shown by plotting the quantity $\frac{n_s * v_s}{v_0}$ versus $\frac{w-2h}{d}$. Let us mention that this argument remains qualitative, although it has the merit to show where the optimum of efficiency should come from.

In summary, the above results show a complex nature of SEAS mixing enhancement mechanism, namely in terms of interaction between acoustic streaming and the main flow. It is thus necessary to provide a detailed interpretation on the mixing enhancement mechanism by AS with different structures.

Mechanism of SEAS assisted mixing enhancement

We hereby attempt to explain the mixing enhancement mechanism of multiple sharp-edge acoustic streaming mixers, by investigating on the streamline patterns of the streaming flow combined with the main channel flow, see Figure 8. Several parameters can describe the intensity of acoustic streaming, such as maximal streaming velocity, vortex size, disturbance distance, among others (Zhang et al. 2019). Hence, the determination of the crucial driving factors of the mixing process would help to understand the link between streaming and mixing. In a more fundamental aspect, the number of sharp edges, their height, distance, are also influential on the streaming pattern (including intensity). To address these points, we show in Figure 8 a global view of the

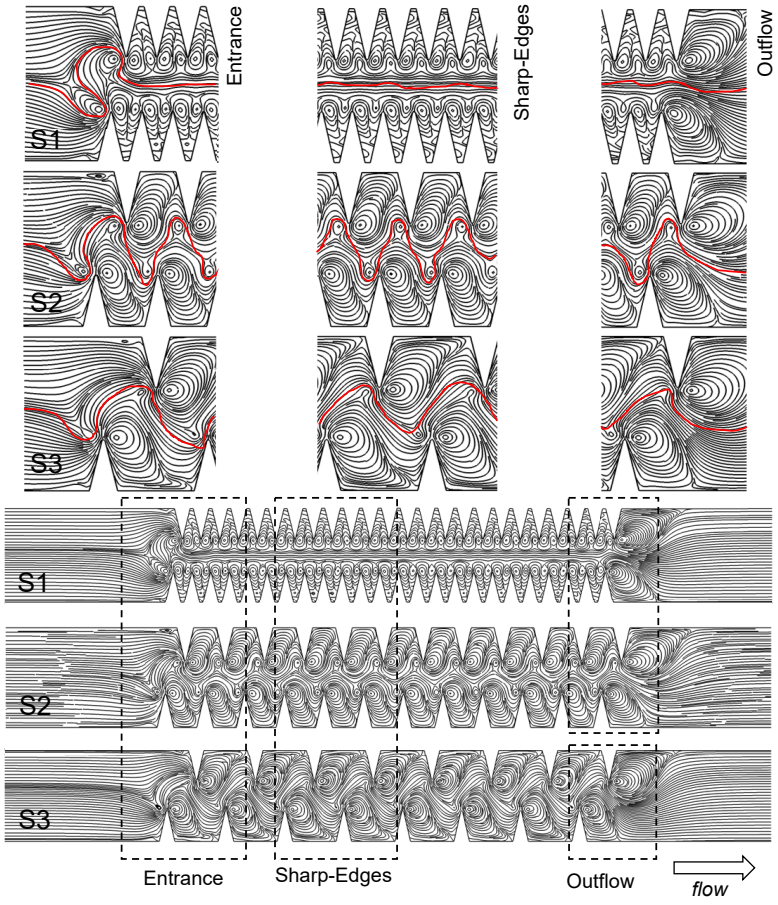

Fig. 8. Streamlines patterns in multiple sharp-edge acoustic streaming, as an explanation support for mixing enhancement. Steady-state velocity streamlines of S1, S2 and S3 (lower figures) under the same condition as in Fig.6. The red line in the zoomed images (upper figures) represents the deflection of the centerline 'interface' between the two fluids. In the spaces between sharp edges, in particular S1, some 'dead zones' appear, where mixing is very limited.

streamlines for the three mixers (lower figures), as well as magnified views on several key locations (upper figures).

The numerical streamline patterns clearly illustrate two main mechanisms of mixing enhancement from acoustic streaming: entrance effect and interactive vortices. These effects can be shown when focusing on three zones chosen as: i) Entrance, ii) Sharp-Edges, and iii) Outflow.

First, the entrance zone before the first sharp-edge is critical for the pre-mixing. For all three mixers, acoustic streaming creates significant transverse velocity component. Due to the space

shift between the sharp edge tips on both sides, the transverse streaming velocity is driven by the first edge and the jet shoots towards the opposite wall. According to the sectional area, the main stream velocity seem the strongest for S1, followed by S2 and S3.

The entrance perturbation appears with a scale as large as the channel width, for all three channels, though the interface of S1 seems to be more serpentine because of smaller d value. This strong perturbation induces the aforementioned transverse jet, thus disturbing the layer between the two fluids. Fast and effective mixing is shown at this entrance zone.

Second, after the entrance, as the fluids continue to flow within the sharp edge section, the size, shape development of vortices and their interaction are main factors that affect mixing. Large vortices have more chance to interact with each other and thus to provide larger contact interface between two mixing fluids. From this point of view, structures with less dense edges (S2 and S3) provide stronger disturbances under the same vibration condition (Fig.8). Conversely, the sharp edges network of S1 is too dense, which does not leave enough space for vortices to develop. Also, S1 shows strong independent self-rotating vortices, competing with those from the opposite edges. This only slightly increases the contact area between the two fluids around a wavy center line as vortices are squeezed into narrow spaces.

After the final sharp edge, the streamlines appear as two large vortices, both joining the main flow. They are much larger than the vortices in the sharp edge zone for S1. For S2 and S3, their size is more comparable size as those in the mixing area.

Finally, it is worth noting that we used uniform-density streamline pattern in Fig.8 and in this case, even the dead zones are filled with streamlines. However, a detailed observation shows that the streamlines in the dead zones of S1 are disconnected with the main stream, which testifies again the inefficiency for mixing. Comparatively, no dead zone can be observed for S2 and S3 since all acoustic streaming jets and vortices extend their influence into the space between two consecutive edges along the opposite wall. This is another reason, though not the main one, why the mixing of S2 and S3 is more efficient than that of S1.

To sum up, the above interpretation constitutes a step forward in understanding the multiple

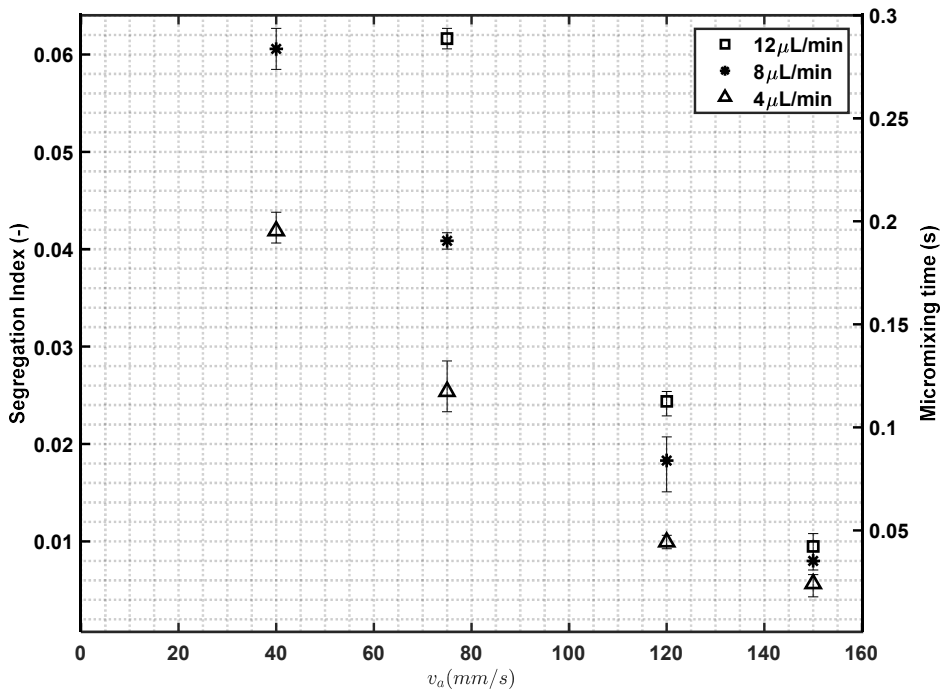

Fig. 9. Micromixing performance of SEAS S2 mixer under different flow-rate and acoustic intensities. Segregation index and Micromixing time are shown respectively at the left- and right-axis. Acoustic intensity is controlled by the input voltage to the piezoelectric actuator, for a range of 10 V, 20 V, 30 V and 40 V, corresponding to acoustic vibration magnitude of v_a from 40-150 mm/s. Error bars are determined by repeated tests for each condition.

SEAS flow on mixing.

Micromixing performance

Since S2 appears to be the most effective SEAS mixer, we keep it to evaluate the micromixing performance, using the experimental method detailed above. Figure 9 shows values of X_S (left axis) and t_m (right axis) versus vibration amplitude v_a, for the mixer S2, and for three different flow-rates Q_c. Firstly, as acoustic intensity v_a increases, X_S and t_m sharply drop, which suggests the achievement of better micromixing performance at the molecular scale. The Segregation Index sharply decreases from 0.06 (at v_a=40 mm/s) down to 0.01 under the strongest acoustic intensity (v_a=150 mm/s). Micromixing time based on IEM decreases by a factor of 10: from 0.28 s under mild forcing (v_a=40 mm/s, at 10 V) to 0.03 s under strong acoustic vibration (v_a=150 mm/s at 40 V).

Another influential factor is the flow-rate Q_c. As shown in Figure 9, a lower channel throughput Q_c corresponds to lower X_S and shorter t_m, thus to better micromixing. This results are in agreement with our previous study (Zhang et al. 2019), according to which each SEAS vortex shape and perturbative potential is strongly influenced by the throughput. As Q_c gets higher, the disturbance from the streaming flow on the main one decays, resulting in worse mixing performance. Similarly, the differences of values of X_S and t_m with different throughput are significant. Under weak acoustic field and high throughput, the mixing improvement becomes weak or even negligible.

Notably, the trend of SEAS micromixing performance with respect to Q_c is the opposite to that of passive mixers such as (Commenge and Falk 2011; Falk and Commenge 2010; Guo et al. 2013). Indeed, passive devices depend on the generation of complex streamlines that in turn can induce Lagrangian chaos. Most often, passive mixers are more efficient under higher throughput.

Regarding the tubing, its effect is shown to be negligible. As shown in Fig.9, without input voltage, the mixer associated with tubing results in too high concentration of I_3^- to be measured by the spectrometer (A = 3, and A is Absorbance Unit, shown in Appendix.I, corresponding $X_S = 0.64$ in Fig.9). Once the acoustic transducer is switched on, however, a sharp decrease of I_3^- concentration can be detected. This proves the main mixing enhancement section of the whole structure is the SEAS mixer and not the tubing part. In addition, our previous study (Guo et al. 2013) showed that the competitive reactions are usually far more rapid than the sampling and waiting time. Thus before the effluent arrives in the sampling cuvette, the mixing process should be already finished.

Micromixing performance comparison with the literature

We now attempt to compare the performance of our micromixers with those of passive mixers on comparable geometries. The review paper (Falk and Commenge 2010) summarized several passive micromixers and proposed a fair agreement between experimental data and a theoretical relation $\frac{t_m}{d_c^2} \sim \frac{ln(Pe)}{Pe}$, with d_c being the characteristic channel dimension. Figure 10 shows the performances of our SEAS mixer S2 with respect to the theoretical line $\frac{t_m}{d_c^2} \sim \frac{ln(Pe)}{Pe}$, with the x-axis being Re. It clearly shows that the SEAS mixer is capable of achieving much faster micromixing that usual passive ones at relatively low Re (lower than one). The quantity t_m/d_c^2 of all tested data ranges

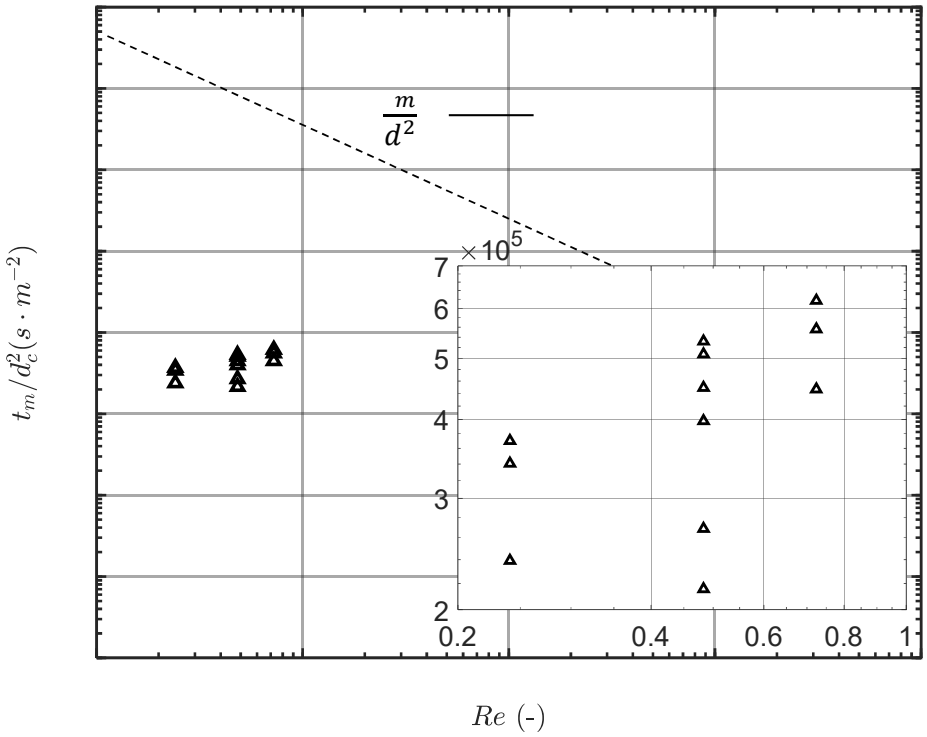

Fig. 10. Quantity t_m/d_c^2 versus channel Reynolds number.

from $2\times10^5 s/m^2$ to $6\times10^5 s/m^2$. Comparatively, at this range, mixing without acoustic streaming is almost purely diffusive and t_m/d_c^2 of passive mixers is of the order of molecular diffusion time 1/D, i.e., $0.4\times10^9 s/m^2$ for water.

The energy consumption in the mixing performance improvement is a crucial factor, both for passive and active mixers. In classical passive mixer studies, a well established method consist in using specific energy dissipate rate as an measurement of energy input. The comparison is thus possible with micromixing time obtained from Iodide-Iodate reaction and the specific energy dissipation rate obtained either by experimental pressure loss ΔP or by numerical simulation through CFD (Commenge and Falk 2011). In the case of passive mixers, the specific energy dissipation rate is expressed as ε_p, (in W/kg) given by:

$$\varepsilon_p = \frac{Q_c \cdot \Delta P}{\rho \cdot V} \tag{12}$$

with Q_c the channel volume throughput, m^3/s, V the internal volume of micromixing, including the inlet and outlet tubing parts, m^3, and ΔP pressure loss in Pa. This energy is supposedly exactly balanced by viscous dissipation.

(Commenge and Falk 2011) summarized a large number of micromixing experimental studies according to which a well established correlation exists between t_m and the specific pumping power dissipation ε_p, see Eq.(13).

$$t_m = 0.15\varepsilon_p^{-0.45} \tag{13}$$

In the case of SEAS mixers, the energy dissipation include both passive (pressure drop) and active mechanisms (acoustic field). The energy dissipation rate (W/kg) thus includes active and passive parts:

$$\varepsilon = \varepsilon_p + \varepsilon_a = \frac{Q_c \Delta P}{\rho V} + \pi f {v_a}^2 sin(4\pi f t) \tag{14}$$

where the first term ε_p represents the energy dissipated into the fluid and is time-independent. The second term $\varepsilon_a = \frac{1}{\rho V}\int_V \partial_t(\frac{1}{2}\rho v_\omega^2)dV = \pi f {v_a}^2 \sin(4\pi f t)$, referring to the definition in (Muller et al. 2012), is estimated as its maximum value $\varepsilon_{a,max} = \pi f {v_a}^2$. More importantly, though, as the characterized length of our SEAS mixer is much smaller than the vibration wavelength in kHz-level, acoustic energy is not dissipated into the liquid but travelling through it. It is thus not strictly totally used to enhance the mixing, although it is necessary to generate the streaming. In our estimation, we use numerical pressure drop results (ranging from 71 Pa to 421 Pa, including channel and bending but without the Y part, corresponding throughput Q_c from 2 to 12 µL/min) through the channel to determine the pumping energy dissipation rate ε_p.

Figure 11 gives the relative positioning of our experimental dissipation rate results with respect to the theoretical correlation between t_m and ε. For a micromixing time range t_m = 0.03 to 0.28 s, classic passive mixer would require a specific energy dissipation rate ε from 0.25 to 27 W/kg. With experimental throughputs using SEAS micromixer S2, the viscous dissipation rate ε_p is from 4×10^{-5} to 2×10^{-3} W/kg, far lower than the range of passive mixers. However, as the real mixing

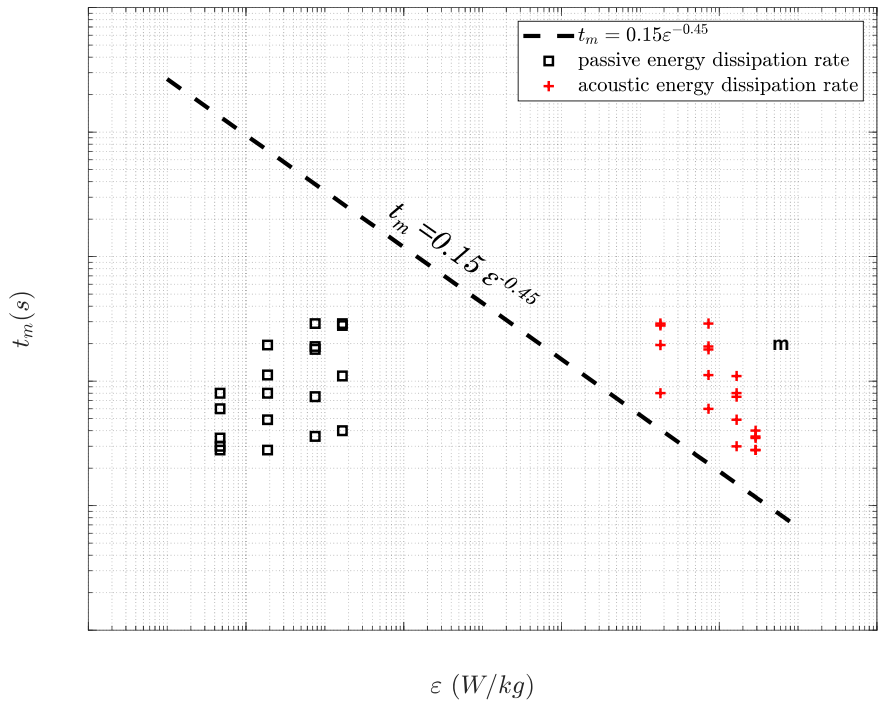

Fig. 11. Micromixing time t_m vs energy dissipation rates ε

enhancement driver, acoustic power with maximal values $\varepsilon_{a,max}$ from 18 to 289 W/kg is necessary. Thus the pressure related dissipation rate in the case of SEAS mixer can be considered negligible compared to the acoustic power. At this stage, as we overestimate the acoustic power, the active SEAS mixer is not yet competitive with passive mixers in terms of specific energy dissipation rate. The real acoustic energy dissipation rate ε_a should be lower than the values shown in Figure 11, thus closer to passive mixers. In addition, under the same acoustic conditions, rigorous optimization of geometrical structure or lager area ratio of sharp edges to the whole channel could further increase the energy efficiency.

CONCLUSIONS

Acoustic streaming is generated near sharp edges along a microchannel, under low-frequency acoustic wave excitation. The disturbances due to the streaming flow actively enhance the mixing process between two miscible fluids injected at the inlets of a Y-mixer. The micromixing would otherwise be achieved through slow diffusion, due to the low Reynolds number flow - from 0.12

to 0.72. However when SEAS is actuated, the generated vortices strengthen the mixing process. Microchannel SEAS mixer with multiple sharp edges can achieve effective mixing but requires optimal coupling between acoustic streaming and main flow, which is the focus of the current study.

The main findings from our results are:

- With a given microchannel, mixing performance depends on i) acoustic intensity, characterized by acoustic velocity amplitude v_a, which itself depends on the driving input voltage V_{pp}; ii) sharp-edge pattern, including number of sharp edges and pitch distance; and iii) channel throughput Q_c.
- More specifically, the performance of multiple SEAS micromixers depends on the interaction between the different AS vortices, as well as the specific flow pattern in the area upstream of the sharp edges. The *entrance effect* sometimes plays an important role to preset the mixing process. In addition, the streamlines patterns confirm the presence of inefficient streaming or dead zones in the case of non-optimal sharp edge design.
- Comparing three different sharp edge patterns, a sufficient number of highly disturbed zigzag flow make SEAS mixer S2 the best in mixing performance. It corresponds to the situation where the ratio of velocities v_s/v_0 realises a matching geometrical condition with the pitch between edges and the channel width.
- Stronger acoustic excitation results in better mixing performance. With V_{pp} increasing from 10 V to 40 V, the best mixing performance using S2 enables X_S and t_m to decrease from 0.06 to 0.01 and from 0.28 s to 0.03 s, respectively. Thus, SEAS achieves much better micromixing performance at high acoustic input. At low acoustic intensity (for instance $V_{pp} = 10$ V, a larger number of sharp edges and a lower throughput Q_c are required to achieve relatively low X_S and short t_m.
- As an active mixer, a SEAS mixer has better performance at low Re (flow rate) when the residence time is long enough and the vortices disturbance is relatively strong compared to the main flow. With Re lower than 1, we did not observe any passive enhancement effect only due to sharp edges in the channel. Without acoustic actuation, the Reynolds number is

too low so that the flow cannot generate significant stretching and folding of the interfacial area between the two fluids. The SEAS mixer thus provides a competitive micromixing solution at low Reynolds regimes.

Further research is still necessary to achieve higher levels of maturity in the use of SEAS micromixer. One of the fundamental aspects is the vibration transmission efficiency from the piezoelectric transducer to the microfluidic channel. Based on our study, the current micromixer does not make use of the acoustic field to its maximal extent due to the relatively short length of the channel. To improve the use of acoustic fields, a promising method could be to increase the length of the channel and the sharp edge area.

ACKNOWLEDGEMENTS

We would like to thank the China Scholarship Council for the financial support to the PhD of Chuanyu Zhang.

APPENDIX I. COMPETITIVE IODIDE-IODATE CHEMICAL REACTION AND DATA PROCESSING

Competitive Iodide-Iodate chemical reaction, also named the Villermaux-Dushman method (Fournier et al. 1996), has been extensively used to evaluate micromixing performance of micromixers (Falk and Commenge 2010; Aubin et al. 2010). This reaction scheme is sensitive to mixing at the molecular level through the formation of Iodine (I_2) molecules. This method is based on the competitive parallel reactions involving the neutralization of dihydroborate ions (R1, Eq.15) and a redox reaction (R2, Eq.16):

$$H_2BO_3^- + H^+ \rightleftharpoons H_3BO_3 \tag{15}$$

$$5\,I^- + IO_3^- + 6\,H^+ \rightleftharpoons 3I_2 + 3\,H_2O \tag{16}$$

$$I_2 + I^- \rightleftharpoons I_3^- \tag{17}$$

Once the molecular Iodine is generated (due to ineffective mixing), a equilibrium is established between the iodine and the iodide ion that results in the formation of the tri-iodide ion, I_3^-, through R3 (Eq.17).

Reactions R1 and R3 are quasi-instantaneous; while reaction R2 is by several orders of magnitude slower than the two others. Within a perfect mixing process, the product distribution is solely governed by the chemical kinetics and most H^+ are consumed by $H_2BO_3^-$, resulting in no or very small iodine yields. On the other hand, a significant amount of iodine occurs under a bad mixing conditions, which can be attributed to a local excess of H^+, not only being consumed by reaction R1, but also taking part in the reaction R2 and R3. Under the later condition, tri-iodide appears in the final product and its concentration can characterize the micromixing process. With an absorption peak to ultraviolet (UV) light at a wavelength of 353 nm, the tri-iodide formation can be quantita-

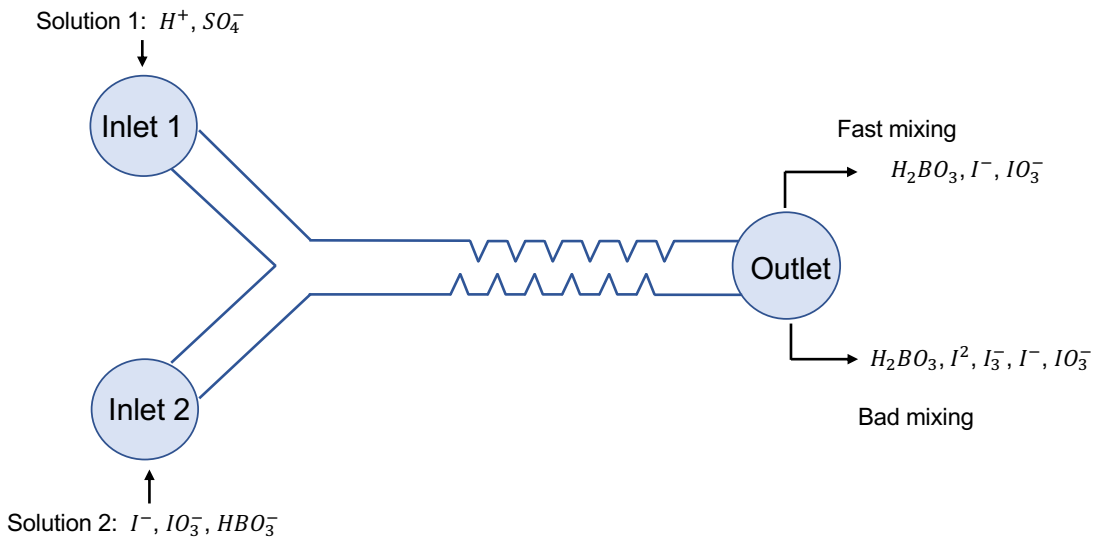

Fig. 12. Sketch of Iodide-Iodate reactions used to micromixing characterization of SEAS micromixers.

tively measured by a spectrophotometer. The whole process is thus considered as a chemical probe to assess the micromixing time. It should be noted that, as for dissociation process of sulfuric acid H_2SO_4, its dissociation constants are $K_{a1} = 1 \times 10^2$ and $K_{a2} = 1 \times 10^{-2}$ respectively for its two-step dissociation process ($H_2SO_4 \rightleftharpoons H^+ + HSO_4^-$ and $HSO_4^- \rightleftharpoons H^+ + SO_4^{2-}$), which are much larger than that of neutralization of dihydroborate ions, $H_3BO_3 \rightleftharpoons H^+ + H_2BO_3^-$, $K_a = 5.8 \times 10^{-10}$. This means that almost no HSO_4^- left in the final solution whether the mixing process is good or not, so the influence of the dissociation equilibrium of sulfuric acid can be neglected in this study.

Figure 12 describes the competing reaction mechanism in the case of our SEAS micromixer with two inlets (solution 1 and solution 2, with the same flow-rate). The concentration of H^+ in solution 1 being equivalent or lower than that of $H_2BO_3^-$, all H^+ is consumed by $H_2BO_3^-$ by the rapid reaction R1 as long as the micromixing process is fast. This results in no iodine formation. On the other hand, iodine formation occurs under bad mixing conditions, which can be attributed to a local excess of H^+, not only being consumed by reaction R1, but also taking place in the reaction R2, followed by R3. The concentration of I_3^- is thus positively correlated to the micromixing time.

Beer-Lambert Law

The tri-iodide can be quantified based on the Beer-Lambert Law, which relates the attenuation of light intensity to the absorption properties of materials through which light travels. To determine its concentration from the absorbance unit given by spectrophotometer, we use the classical relation :

$$C_{I_3^-} = A/\epsilon_{353nm} l \tag{18}$$

where A is the Absorbance Unit through the cuvette, (-), ϵ_{353nm} means the molar attenuation coefficient of tri-iodide ions at its peak absorptivity wave-length at 353 nm, $\epsilon_{353nm} = 26047 L/(mol.cm)$, l denotes the optical path length which is $l = 10mm$ in our case.

Calculation of Y and Y_{ST}

Calculation of Y and Y_{ST} from the concentration of reactants as well as that of the tri-iodide yield follows Eqs.19 and 20 (Guo et al. 2013). More specifically, Y is the ratio of acid ion H^+ consumed by reactions R2 and R3 and its initial concentration in the mixture. The quantity C represents the concentration of ions while Q_1 and Q_2 stand for the flow rates of the two solutions, in this study $Q_1 = Q_2$, Y_{ST} is the higher limit of Y in the total segregation case, also based on the initial boric acid and iodate ions concentrations.

$$Y = \frac{2(\mathrm{M}_{\mathrm{I}_2} + \mathrm{M}_{\mathrm{I}_3^-})}{M_{\mathrm{H}^+,0}} = \frac{2(C_{\mathrm{I}_2} + C_{\mathrm{I}_3^-})(Q_1 + Q_2)}{2C_{\mathrm{H_2SO_4}} Q_2} \tag{19}$$

$$Y_{ST} = \frac{6M_{\mathrm{IO}_3^-,0}/M_{\mathrm{H_2BO}_3^-,0}}{6M_{\mathrm{IO}_3^-,0}/M_{\mathrm{H_2BO}_3^-,0} + 1} = \frac{6C_{\mathrm{IO}_3^-,0} Q_1}{(6C_{\mathrm{IO}_3^-,0} + C_{\mathrm{H_2BO}_3^-,0}) Q_1} \tag{20}$$

With the yield of tri-iodide ions in the final solution, the production of iodine can be determined based on the equilibrium balance of I in R3 Eq.(17):

$$M_{I^-} = M_{I^-,0} - \frac{5}{3}(M_{I_2} + M_{I_3^-}) - M_{I_3^-} \tag{21}$$

$$C_{I^-} = \frac{C_{I^-,0}}{2} - \frac{5}{3}(C_{I_2} + C_{I_3^-}) - C_{I_3^-} \tag{22}$$

with the equilibrium kinetics of reaction R3 given by Eq.(23).

$$-\frac{5}{3}C_{I_2}^2 + (\frac{C_{I^-,0}}{2} - \frac{8}{3}C_{I_3^-})C_{I_2} - \frac{C_{I_3^-}}{K_{eq}} = 0 \tag{23}$$

Then X_S is calculated from Eq.(2).

Reaction kinetics

Thee kinetics for each reaction are listed below (Guichardon and Falk 2000) and they will be used in the IEM model.

$$r_1 = k_1 C_{H^+} C_{H_2BO_3^-} \tag{24}$$

$$r_2 = k_2 C_{H^+}^2 C_{I^-}^2 C_{IO_3^-} \tag{25}$$

$$r_3 = k_{3+} C_{I^-} C_{I_2} - k_{3-} C_{I_3^-} \tag{26}$$

where the k_i stand for the kinetics constants of each reaction. For r_2, fifth-order law are used in the present study. The coefficients k_{3+} and k_{3-} are the forward and reverse reaction rate constants, being respectively equal to $k_{3+} = 5.9 \times 10^9 L \cdot (mol \cdot s)^{-1}$ and $k_{3-} = 7.5 \times 10^6 s^{-1}$ at 25°C.

For reaction R1, as a neutralization reaction, its rate constant is $k_1 = 10^{9.2}\ L \cdot (mol \cdot s)^{-1}$, determined by its acid dissociation constant with Eq.(27).

$$\log_{10}(k_1) = pK_a(H_3BO_3/H_2BO_3^-) = 9.2 \tag{27}$$

The rate constant k_2 of redox reaction R2 is a function of the ion strength μ of ions in the

solution. It is determined by Eqs.(29-30) after Eq.(28).

$$\mu = \frac{1}{2}\sum C_i Z_i^2 \tag{28}$$

$$\log_{10}(k_2) = 9.28105 - 3.664\sqrt{\mu} \qquad if\,\mu < 0.166 mol/L \tag{29}$$

$$\log_{10}(k_2) = 8.383 - 1.5115\sqrt{\mu} + 0.23689\mu \qquad if\,\mu >= 0.166 mol/L \tag{30}$$

where C_i and Z_i denotes the concentration and charges of i_{th} specie in the solution.

The equilibrium constant of reaction R3 can be determined by:

$$\frac{\mathrm{C_{I_3^-}}}{\mathrm{C_{I_2}\,C_{I^-}}} = \log_{10}(k_{eq}) = \log_{10}\frac{k_{3+}}{k_{3-}} = \frac{555}{T} + 7.355 - 2.575\log_{10} T \tag{31}$$

where T is temperature in Kelvin. At 25 ℃, $k_{eq} = 698\ L \cdot mol^{-1}$.

APPENDIX II. DETERMINATION OF MICROMIXING TIME

Interaction by Exchange with the Mean (IEM) model is usually used to build up the relation between Segregation Index and micromixing time. The IEM allows the estimation of the micromixing time (Guo et al. 2013; Falk and Commenge 2010), and makes them independent of the choice of concentration of reactants (Commenge and Falk 2011). The comparison of mixing results is thus possible. One prerequisite of using IEM model is that the residence time of the two solutions from the initial contact and along flow direction being the same. Our sharp edge Y-mixer satisfies this requirement. Besides, another assumption in this model is that the exchange of ions between two solutions occurs at a same micromixing time t_m, which is generally true for microchannel continuous mixers.

At every time step, IEM considers that the concentration of each solution evolves separately and is governed by the following equations:

$$\frac{dC_{k,1}}{dt} = \frac{\overline{C} - C_{K,1}}{t_m} + R_{k,1} \tag{32}$$

$$\frac{dC_{k,2}}{dt} = \frac{\overline{C} - C_{K,2}}{t_m} + R_{k,2} \tag{33}$$

$$\overline{C} = \alpha_v C_{k,1} + (1 - \alpha_v) C_{k,2}, \tag{34}$$

where the coefficient $C_{k,1,2}$ represent the concentration for specie k in solution 1 and 2, mol/L; t_m is the exchange time constant, considered as the micromixing time, s; $R_{k,1,2}$ denotes the change rate of the concentration for species k in solution 1 and 2, $mol/(L \cdot s)$; α_v the volume flow proportion of solution 1, in our case $\alpha_v = 0.5$.

With a given t_m and known initial concentrations of ions, the differential equations can be numerically integrated based on the second-order Runge-Kutta method or an equivalent one, to determine the final concentration $C_{I_3^-}$ and then the value for X_S. For each step, the concentrations and their corresponding mean values, kinetic data are updated by the results from the previous step. The iteration process moves forward step by step until the concentration of H^+ in the solution

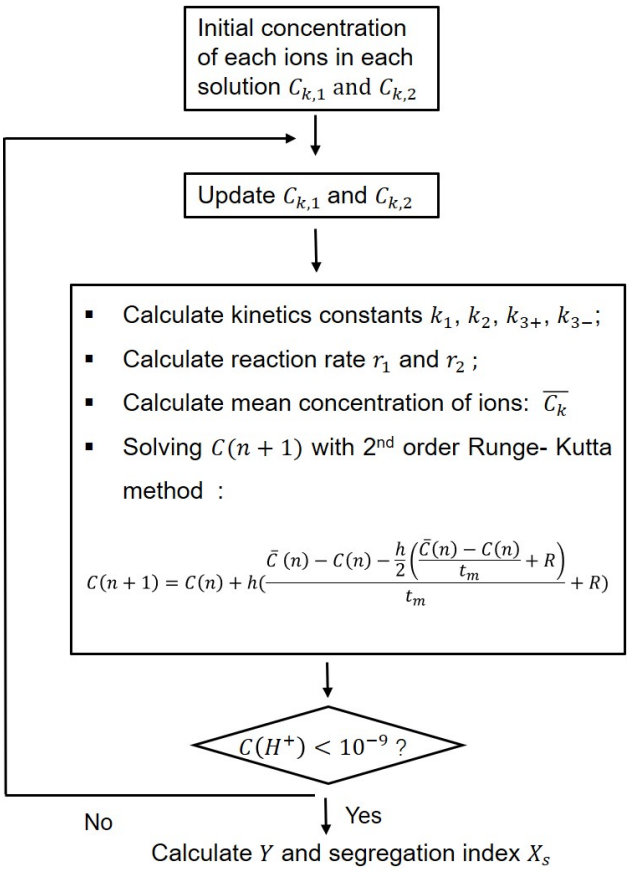

Fig. 13. Algorithmic steps for identifying the relationship between X_S and t_m using IEM model

decrease under a lower threshold value ($10^{-9} mol/L$ in this study). After, H^+ is considered to approach zero and the reactions end. With $C_{I_3^-}$, X_S can be calculated accordingly. An algorithm has been built in Matlab to relate the segregation index with the micromixing time in a large range. This procedure and the resulting relation between X_S and t_m under the concentration condition are shown respectively in Figures 13 and 14. As a result, for each micromixing tests, the segregation index and the corresponding micromixing time can be quantified.

Special attention should be paid on the iteration time step h. On the one hand, the step h should be small enough to avoid unrealistic negative concentrations due to global consumption of ions in the reactions; on the other, a too short time step requires heavier computing costs. In this study, h is kept constant as $10^{-8} s$.

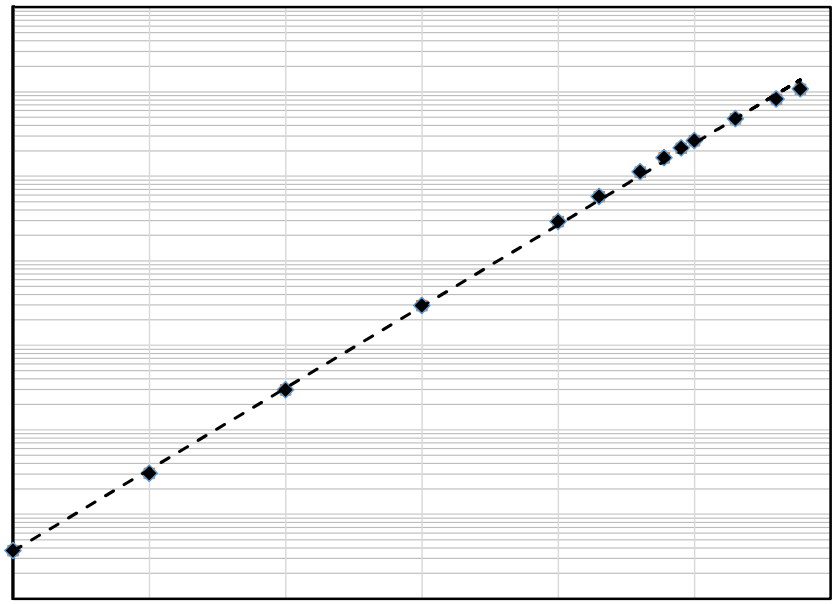

Fig. 14. Segregation index X_S versus micromixing time t_m, for given values of concentrations in Table 1.

APPENDIX III. NOTATION

The following symbols are used in this paper:

Quantity	Abbreviation
Absorbance unit from spectrophotometry	A
Tip angle of sharp edge	α
Height of the sharp edge	h
Width of microchannel	w
Distance between the tip of two consecutive edges on the same side	d
Number of the sharp edges on one side	n_s
Kinematic viscosity	ν
Diffusivity	D
Acoustic vibration velocity	$\mathbf{v}_\omega$
Amplitude of vibration velocity	$\mathbf{v}_a$
Streaming velocity	$\mathbf{v}_s$
Amplitude of vibration velocity at boundary	$\mathbf{v}_{ab}$
Boundary velocity corresponding to channel throughput	$\mathbf{v}_{0b}$
Maximum streaming velocity along y direction	$\mathbf{v}_{sm}$
Concentration	C
Resonance frequency	f
Angular frequency	ω
Molar quantity of reactants or ions	M
Characteristic channel dimension	d_c
Inlet flow rate	Q_c
Peak to peak voltage	V_{pp}
Segregation Index	X_S
Micromixing time	t_m
Pumping energy dissipation rate	ε_p
Acoustic energy dissipation rate	ε_a
Péclet number	Pe
Reynolds number	Re

REFERENCES

Aubin, J., Ferrando, M., and Jiricny, V. (2010). "Current methods for characterizing mixing and flow in microchannels.." Chemical Engineering Science, 65(6), 2065–2093.

Bachman, H., Chen, C., Rufo, J., Zhao, S., Yang, S., Tian, Z., Nama, N., Huang, P.-H., and Huang, T. J. (2020). "An acoustofluidic device for efficient mixing over a wide range of flow rates." Lab on a Chip, 20(7), 1238–1248.

Bruus, H. (2012). "Acoustofluidics 10: Scaling laws in acoustophoresis." Lab on a Chip, 12(9), 1578.

Commenge, J.-M. and Falk, L. (2011). "Villermaux–Dushman protocol for experimental character-

ization of micromixers." Chemical Engineering and Processing: Process Intensification, 50(10), 979–990.

DeMello, A. J. (2006). "Control and detection of chemical reactions in microfluidic systems." Nature, 442(7101), 394–402.

Doinikov, A. A., Gerlt, M. S., and Dual, J. (2020a). "Acoustic Radiation Forces Produced by Sharp-Edge Structures in Microfluidic Systems." Physical Review Letters, 124(15), 154501.

Doinikov, A. A., Gerlt, M. S., Pavlic, A., and Dual, J. (2020b). "Acoustic streaming produced by sharp - edge structures in microfluidic devices." Microfluidics and Nanofluidics, 1–13.

Dong, Z., Yao, C., Zhang, X., Xu, J., Chen, G., Zhao, Y., and Yuan, Q. (2015). "A high-power ultrasonic microreactor and its application in gas–liquid mass transfer intensification." Lab on a Chip, 15(4), 1145–1152.

Falk, L. and Commenge, J. M. (2010). "Performance comparison of micromixers." Chemical Engineering Science, 65(1), 405–411.

Fournier, M. C., Falk, L., and Villermaux, J. (1996). "A new parallel competing reaction system for assessing micromixing efficiency - Experimental approach." Chemical Engineering Science, 51(22), 5053–5064.

Guichardon, P. and Falk, L. (2000). "Characterisation of micromixing efficiency by the iodide–iodate reaction system. Part I: experimental procedure." Chemical Engineering Science, 55(19), 4233–4243.

Guo, X., Fan, Y., and Luo, L. (2013). "Mixing performance assessment of a multi-channel mini heat exchanger reactor with arborescent distributor and collector." Chemical Engineering Journal, 227(0), 116–127.

Guo, X., Fan, Y., and Luo, L. (2014). "Multi-channel heat exchanger-reactor using arborescent distributors: A characterization study of fluid distribution, heat exchange performance and exothermic reaction." Energy, 69(0), 728–741.

Hossain, S., Husain, A., and Kim, K. Y. (2010). "Shape optimization of a micromixer with staggered-herringbone grooves patterned on opposite walls." Chemical Engineering Journal,

162(2), 730–737.

Huang, P.-H., Xie, Y., Ahmed, D., Rufo, J., Nama, N., Chen, Y., Chan, C. Y., and Huang, T. J. (2013a). "An acoustofluidic micromixer based on oscillating sidewall sharp-edges." Lab on a Chip, 13(19), 3847.

Huang, P. H., Xie, Y., Ahmed, D., Rufo, J., Nama, N., Chen, Y., Chan, C. Y., and Huang, T. J. (2013b). "An acoustofluidic micromixer based on oscillating sidewall sharp-edges." Lab on a Chip, 13(19), 3847–3852.

Hutchisson, E. and Morgan, F. B. (1931). "An experimental study of Kundt's tube dust figures." Physical Review, 37(9), 1155–1163.

Leaist, D. G. (1988). "The effects of aggregation, counterion binding, and added NaCl on diffusion of aqueous methylene blue." Canadian Journal of Chemistry, 66(9), 2452–2457.

Lei, J., Glynne-Jones, P., and Hill, M. (2013). "Acoustic streaming in the transducer plane in ultrasonic particle manipulation devices." Lab on a Chip, 13(11), 2133.

Li, W., Xia, F., Qin, H., Zhang, M., Li, W., and Zhang, J. (2019). "Numerical and experimental investigations of micromixing performance and efficiency in a pore-array intensified tube-in-tube microchannel reactor." Chemical Engineering Journal, 370, 1350–1365.

Li, Z. and Kim, S. J. (2017). "Pulsatile micromixing using water-head-driven microfluidic oscillators." Chemical Engineering Journal, 313, 1364–1369.

Lighthill, S. I. R. J. (1978). "ACOUSTIC STREAMINGt." Journal of Sound And Vibration, 61(April), 391–418.

Luo, Y., Luo, J. Z., Yue, X. J., Song, Y. J., Chu, G. W., Liu, Y., Le, Y., and Chen, J. F. (2018). "Feasibility studies of micromixing and mass-transfer in an ultrasonic assisted rotating packed bed reactor." Chemical Engineering Journal, 331, 510–516.

Muller, P. B., Barnkob, R., Jensen, M. J. H., and Bruus, H. (2012). "A numerical study of microparticle acoustophoresis driven by acoustic radiation forces and streaming-induced drag forces." Lab on a Chip, 12(22), 4617–4627.

Nam, J., Jang, W. S., and Lim, C. S. (2018). "Micromixing using a conductive liquid-based focused

surface acoustic wave (CL-FSAW)." Sensors and Actuators, B: Chemical, 258, 991–997.

Nama, N., Huang, P. H., Huang, T. J., and Costanzo, F. (2016). "Investigation of micromixing by acoustically oscillated sharp-edges." Biomicrofluidics, 10(2).

Orbay, S., Ozcelik, A., Lata, J., Kaynak, M., Wu, M., and Huang, T. J. (2017). "Mixing high-viscosity fluids via acoustically driven bubbles." J. Micromech. Microeng, 27(44), 15008.

Ovchinnikov, M., Zhou, J., and Yalamanchili, S. (2014). "Acoustic streaming of a sharp edge." The Journal of the Acoustical Society of America, 136(1), 22–29.

Ozcelik, A., Ahmed, D., Xie, Y., Nama, N., Qu, Z., Nawaz, A. A., and Huang, T. J. (2014). "An acoustofluidic micromixer via bubble inception and cavitation from microchannel sidewalls." Analytical Chemistry, 86(10), 5083–5088.

Qin, H., Zhang, C., Xu, Q., Dang, X., Li, W., Lei, K., Zhou, L., and Zhang, J. (2017). "Geometrical improvement of inline high shear mixers to intensify micromixing performance." Chemical Engineering Journal, 319, 307–320.

Rayleigh, J. W. S. (2013). The Theory of Sound, Volume One. Dover Publications, <http://cds.cern.ch/record/105679>.

Rezk, A. R., Qi, A., Friend, J. R., Li, W. H., and Yeo, L. Y. (2012). "Uniform mixing in paper-based microfluidic systems using surface acoustic waves." Lab on a Chip, 12(4), 773–779.

Setareh, M., Saffar-Avval, M., and Abdullah, A. (2020). "Heat transfer enhancement in an annulus under ultrasound field: A numerical and experimental study." International Communications in Heat and Mass Transfer, 114, 104560.

Shanko, E. S., van de Burgt, Y., Anderson, P. D., and den Toonder, J. M. (2019). "Microfluidic magnetic mixing at low reynolds numbers and in stagnant fluids." Micromachines, 10(11).

Shilton, R. J., Yeo, L. Y., and Friend, J. R. (2011). "Quantification of surface acoustic wave induced chaotic mixing-flows in microfluidic wells." Sensors and Actuators, B: Chemical, 160(1), 1565–1572.

Sritharan, K., Strobl, C. J., Schneider, M. F., Wixforth, A., and Guttenberg, Z. (2006). "Acoustic mixing at low Reynold's numbers." Applied Physics Letters, 88(5), 1–3.

Stroock, A. D., Dertinger, S. K., Ajdari, A., Mezić, I., Stone, H. A., and Whitesides, G. M. (2002). "Chaotic mixer for microchannels." Science, 295(5555), 647–651.

Vainshtein, B. P. (1995). "Rayleigh streaming at large Reynolds number and its effect on shear flow." 285, 249–264.

Yang, L., Xu, F., Zhang, Q., Liu, Z., and Chen, G. (2020). "Gas-liquid hydrodynamics and mass transfer in microreactors under ultrasonic oscillation." Chemical Engineering Journal, 397, 125411.

Zhang, C., Guo, X., Brunet, P., Costalonga, M., and Royon, L. (2019). "Acoustic streaming near a sharp structure and its mixing performance characterization." Microfluidics and Nanofluidics, 23(9), 104.

Zhang, C., Guo, X., Royon, L., and Brunet, P. (2020a). "Acoustic Streaming Generated by Sharp Edges: The Coupled Influences of Liquid Viscosity and Acoustic Frequency." Micromachines, 11(6), 607.

Zhang, C., Guo, X., Royon, L., and Brunet, P. (2020b). "Unveiling of the mechanisms of acoustic streaming induced by sharp edges." Physical Review E, 102, 043110.

Zhao, S., Dong, Z., Yao, C., Wen, Z., Chen, G., and Yuan, Q. (2018). "Liquid–liquid two-phase flow in ultrasonic microreactors: Cavitation, emulsification, and mass transfer enhancement." AIChE Journal, 64(4), 1412–1423.